Terahertz wide-angle metalens with nearly ideal object-image relation

Yu Wang (王 宇)[1], Jierong Cheng (程洁嵘)[1,2*], Yunyun Ji (冀允允)[1,2], Fei Fan (范 飞)[1,3], and Shengjiang Chang (常胜江)[1,3]

[1] Institute of Modern Optics, Nankai University, Tianjin 300350, China
[2] Tianjin Key Laboratory of Micro-scale Optical Information Science and Technology, Tianjin 300350, China
[3] Tianjin Key Laboratory of Optoelectronic Sensor and Sensing Network Technology, Tianjin 300350, China

*Corresponding author: chengjr@nankai.edu.cn
Received June 21, 2023 | Accepted September 1, 2023 | Posted Online January 8, 2024

Metalenses are essential components in terahertz imaging systems. However, without careful design, they show limited field of view and their practical applications are hindered. Here, a wide-angle metalens is proposed whose structure is optimized for focusing within the incident angles of ±25°. Simulation and experiment results show that the focusing efficiency, spot size, and modulation transfer function of this lens are not sensitive to the incident angle. More importantly, this wide-angle metalens follows the ideal Gaussian formula for the object-image relation, which ensures a wider field of view and better contrast in the imaging experiment.

Keywords: terahertz; metalens; wide-angle; Gaussian formula.
DOI: 10.3788/COL202422.013701

1. Introduction

Since the proposal of the generalized Snell's law[1], the functions of metasurfaces have become increasingly diverse, such as polarization control[2,3], beam deflection[4], holographic imaging[5], and structured light generation[6,7], among which the most promising and closest to practical applications are metalenses[8,9].

By encoding the desired phase modulation into the subwavelength-scale units in the metasurface, ultrathin planar structures can replace conventional curved lenses to achieve flexible wavefront manipulation. The problems of low focusing efficiency and bulky structure of the curved lens are particularly prominent in the terahertz (THz) band due to the longer wavelengths. Therefore, the planar metalens has become the key device in the THz imaging system, and plays an important role in THz beam shaping[10], imaging[11], focusing[12], collimation[13], filtering, and other applications[14].

The basic function of a THz metalens is to focus the incoming plane wave from a specific direction and at a specific frequency into a diffraction-limited spot. Apparently, we are no longer satisfied with this function now, and the study is targeting to high numerical aperture (NA), broadband achromatic aberration, long focal depth, dynamic focusing, and a wide field of view. Dong et al. demonstrated a THz metalens with an NA of 0.94 using low-refractive-index polymer materials based on the nonlocal diffraction modulation mechanism[15]. Wang et al. achieved tight focusing of 2.52 THz radially polarized light using a silicon cylinder metalens with an NA of 0.92[16]. Superoscillating THz metalenses with NA as high as 0.95 and 0.975 have also been proposed[17,18]. Researchers use the combination of solid and complementary hollow dielectric units combinations or sandwich units to realize the THz achromatic metalens[19–21]. Yang et al. realized a THz metalens with subwavelength resolution imaging over a 9.1λ long distance based on the nonlocal diffraction engineering[22]. Xiao et al. proposed a THz metalens with an adjustable focal length of over 100 μm at 1.8–2.2 THz[23]. However, most of these studies are limited to converting normally incident planar beams into focused spherical waves. In order to replace the traditional curved lens to form a perfect imaging system, the metalens needs to have a certain field of view, that is, to effectively focus beams with different incident angles, and to satisfy the classic Gaussian imaging law. Although the double-layer metalens in the optical band can eliminate off-axis aberrations to a good extent[24], there are few reports on wide-angle metalenses in the THz band, and the systematic study of the relation between the object and the image of the metalens is still absent.

Therefore, this paper designs a wide-angle metalens that exhibits a nearly ideal object-image relation in the THz band. The metalens is composed of double-layer nonperiodic concentric rings. The gradient descent algorithm is used to optimize the metalens structure globally to achieve ideal focusing at different incident angles ranging from 0° to 25°. Comparison with the narrow-angle metalens shows that the wide-angle one has more

stable focusing efficiency, similar focused beam width, and diffraction-limited modulation transfer function (MTF) at different incident angles. The object-image relation conforms to the ideal Gaussian formula. The imaging experiment further validates the wide field of view and good imaging quality of the wide-angle metalens. This research provides an effective solution for the development of THz compact imaging systems and is of great significance for promoting the application of THz technology in biomedicine, security detection, and other fields.

2. Metalens Optimization and Fabrication

The metalens is composed of double-layered concentric rings, whose cross section is shown in Fig. 1(a). In order to increase the field of view, the metalens should focus the incoming beam from different directions into the same plane at a distance of f. The offset of the focal point relative to the optical axis is defined as $f \cdot \tan \theta$ for the incident angle of θ. Here we use the gradient descent algorithm combined with the full-wave electromagnetic simulation to automatically generate the whole metalens structure so as to fulfill the focusing requirement at different incident angles. The optimization of the whole aperture can accurately characterize the interactions among ridges, and offer a straightforward way to handle different incident angles.

The dielectric material of the metalens is polylactic acid (PLA), and its refractive index is 1.57 at the target operating frequency of 0.14 THz[25]. PLA is a type of commonly used 3D printing filaments. Therefore, the metalens can be quickly processed at low cost through 3D printing technology. The lens size is 50 mm × 50 mm, and the target focal length is $f = 20$ mm. The metalens has a double-layer concentric ring structure. Based on our previous study[15,25], a double-layer structure is very helpful

for efficient wavefront modulation when the dielectric material shows a low refractive index, as it doubles the number of variables and the number of guided modes. The number of ridges is 100, half of which are in the top layer and the rest in the bottom layer. The ridge-to-ridge distance is 1 mm, and the height of the ridge is fixed as 2 mm. The widths W_i ($i = 1$–100) of the ridges in the top and bottom layers are the variables to be optimized. The target value to be maximized during the optimization is defined as

$$\text{target} = \frac{1}{N} \sum_{i=1}^{N} |E_i(z = f, x = f \cdot \tan \theta_i, \theta_i)|. \quad (1)$$

That is the average value of the electric field intensity E_i at the target focus under different incident angles θ_i. N is the total number of incident angles considered in the optimization. During the optimization, the variables W_i are randomly generated to form the initial metalens structure, which is evaluated by finite-difference time-domain simulation (FDTD Solutions) to calculate the "target" electric field at the focal point. Then the variables are updated based on the nonlinear optimization function *fmincon* in MATLAB to modify the metalens structure[15]. The *fmincon* function is used because it has the advantages of being able to customize a variety of constraint functions and fast optimization speed. When the step size of the variables is smaller than a threshold of 10^{-12}, the iteration will stop, and the optimization converges. For comparison, two metalenses are considered, respectively, with the first one optimized for $\theta = 0°$ and the second one for $\theta = [0°, 5°, 10°, 15°, 20°, 25°]$. For convenience of description, they are called narrow-angle and wide-angle metalenses, respectively. Figure 1(b) shows the evolution of the target value for the two metalenses. The narrow-angle metalens converges faster with a higher target value. This is because the focal spot intensity decreases with the increase of the incident angle. The two metalenses after optimization are 3D printed by the fused deposition modeling method, with a minimum feature size of 0.2 mm. The top and bottom details are shown in Fig. 1(c). The rotation-symmetric structure makes them insensitive to the polarization.
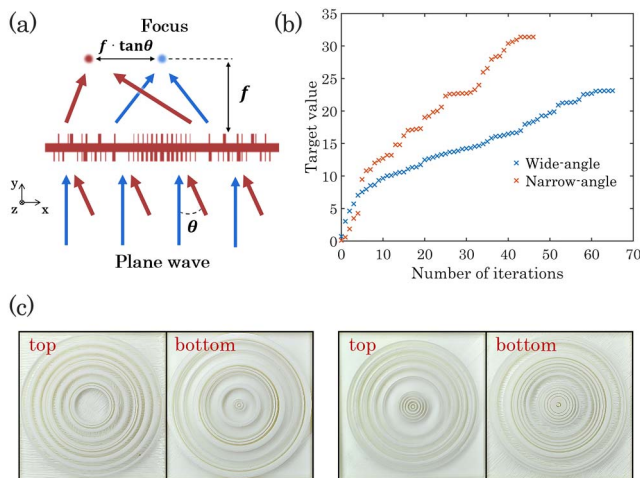
3. Focusing Characterization of the Metalenses

In the following, we study the focusing effects of the two metalenses from the simulation and the experiment. The field distributions after the two metalenses at different incident angles are simulated in Figs. 2(a) and 2(b). The Gaussian beam at 0.14 THz with a beam waist radius of 30 mm is used for excitation. The experimental setup for measuring the field distribution is shown in Fig. 2(e). The source is an IMPATT diode, and the radiation is collimated to be consistent with the simulation setting. The incident angle of the beam is controlled by rotating the metalens, and the Schottky diode detector with a pinhole is scanned by a 3D translation stage. The measured field distributions of the narrow-angle and wide-angle metalenses at different incident angles are shown in Figs. 2(c) and 2(d), with a scanning step size
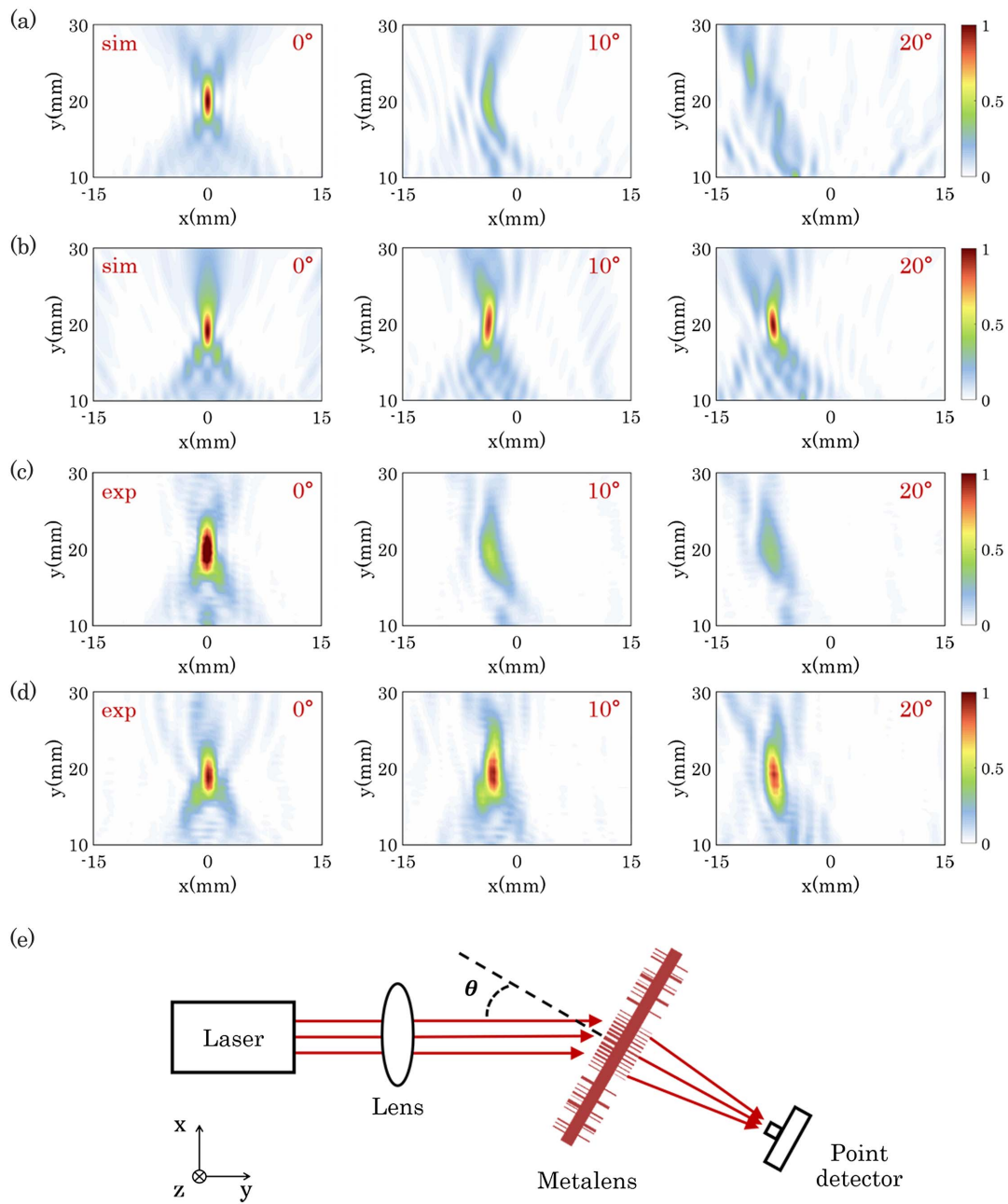

Fig. 1. (a) Schematic diagram of the wide-angle metalens, which focuses the beam from the angle of θ to the focal point with lateral shift of $f \cdot \tan \theta$; (b) evolution of the target value (focal spot peak intensity) with the number of optimization iterations for the wide-angle and narrow-angle metalenses; (c) 3D printed narrow-angle metalens (left) and wide-angle metalens (right).

Fig. 2. (a), (b) Simulated intensity distribution in the x–y plane for (a) the narrow-angle metalens and (b) the wide-angle metalens at incident angles of 0°, 10°, and 20°; (c), (d) measured intensity distribution in the x–y plane for (c) the narrow-angle metalens and (d) the wide-angle metalens at incident angles of 0°, 10°, and 20°; (e) schematic diagram of the experimental setup.

of 0.5 mm. Both the simulation and the experiment show that the narrow-angle metalens only has a good focusing effect for the normally incident wave. When the incident angle goes beyond 10°, the beam cannot be focused. However, the wide-angle metalens shows a clear focus at 0°, 10°, and 20° incident angles, and the focus position conforms to the law of $f \cdot \tan \theta$. The simulation results are consistent with the experimental results.

Further, the focusing efficiency, the focal spot size, and the MTF are quantitatively analyzed. The focusing efficiency is defined as the ratio of the energy within the area of 3 times the FWHM to the total energy[26]. As shown in Fig. 3(a), the wide-angle and narrow-angle metalenses have the focusing efficiency of 50% and 60%, respectively, for normal incidence. With the increase of θ, the efficiency is relatively stable (slightly decreased in experiment) for the wide-angle metalens, while decreasing sharply for the narrow-angle one.

The FWHM of the focal spots of the two lenses is shown in Fig. 3(b). At normal incidence, the two lenses show similar FWHM, which is 1.28 mm (0.6λ) in simulation and 1.8 mm
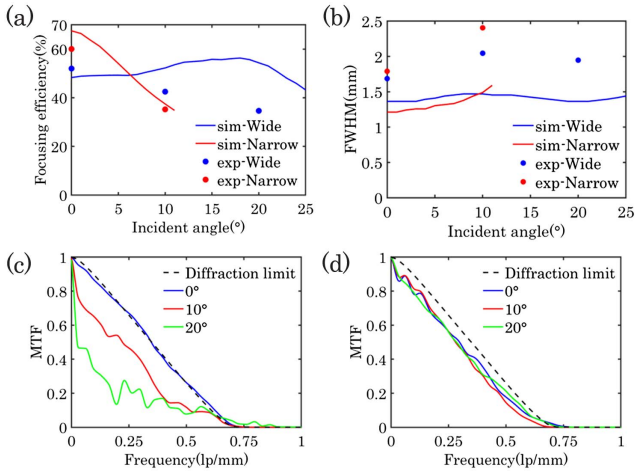
Fig. 3. (a) Focusing efficiency of two metalenses at different incident angles; (b) FWHM of two metalenses; MTF curves of (c) the narrow-angle metalens and (d) the wide-angle metalens.

(0.84λ) in experiment. The broadening in measurement is mainly due to the convolution effect of the finite-size pinhole with the real field distribution. The FWHM of the wide-angle metalens is almost stable with the incident angle θ, and there is no obvious aberration.

In order to better quantify the imaging resolution and off-axis aberration of the metalens, Figs. 3(c) and 3(d) calculate the MTF curves of the two metalenses when the incident angle is 0°, 10°, and 20°, which are obtained by calculating the Fourier transform of the focusing spot[24]. The diffraction-limited MTF is obtained by performing Fourier transform of the diffraction-limited point spread function. The MTF of the narrow-angle metalens under normal incidence approaches the diffraction-limited MTF and drops sharply for oblique incidence, which proves that the lens has a large off-axis aberration. For comparison, the MTF of the wide-angle metalens is quite stable with the incident angle and always follows the diffraction-limited curve. The resolution limit is 0.73 lp/mm for all angles within 20°. The comparison in Fig. 3 shows that the wide-angle metalens slightly sacrifices the focusing efficiency and gains much more stable and diffraction-limited focusing for oblique incidence.

4. Analysis of Object-Image Relation and Imaging

Most of the existing metalenses are designed at a specific excitation condition, such as the plane wave. When the excitation is changed into spherical waves, the response is out of control. The fundamental reason is that the elements of the metalens are incident angle sensitive. This limits the application of the metalens. Here we analyze the object-image relationship to push the performance of the metalens much closer to conventional thin lenses at a single frequency, while gaining a thin and flat structure.

In order to analyze the object-image relation of the metalens, we first build an ideal point source by focusing the collimated
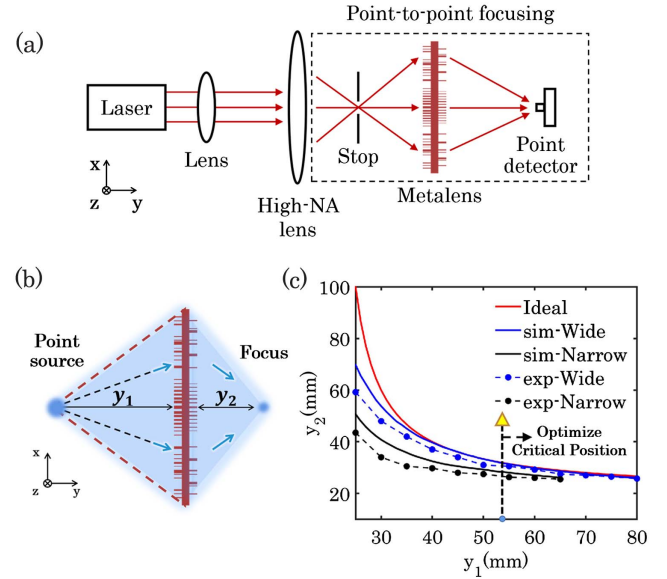

Fig. 4. (a) Experimental setup for testing the object-image relation of the metalens; (b) details of the definition of the object distance and image distance for the point-to-point focusing; (c) on-axis ideal Gaussian object-image relation and the simulated and measured ones for the two metalenses.

THz beam by a high-NA lens, as shown in Fig. 4(a). The tight focus after the high-NA lens is further filtered by stop to behave as a point object.

Then the object distance y_1 is adjusted, and the image distance y_2 is obtained by locating the position of the smallest and strongest imaging spot, as shown in Fig. 4(b). The ideal object-image relation should satisfy the Gaussian formula as
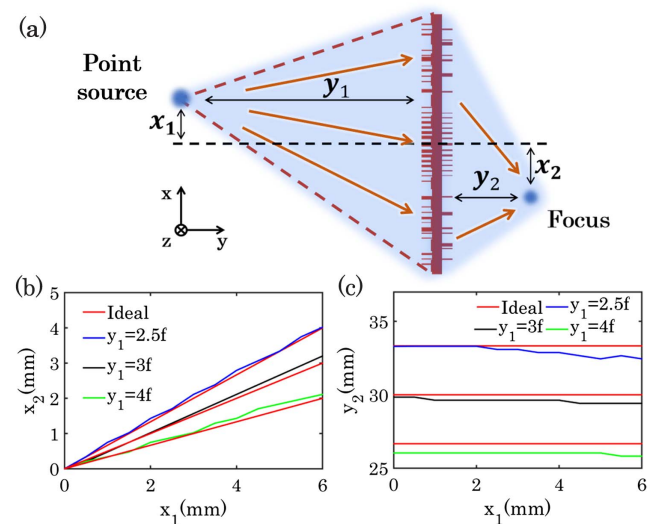
$$\frac{1}{y_1} + \frac{1}{y_2} = \frac{1}{f}. \tag{2}$$

Fig. 5. (a) Schematic diagram of off-axis point-to-point focusing; variation of (b) the image height x_2 and (c) the image distance y_2 for different x_1 and y_1.

Figure 4(c) shows the ideal object-image curve from Eq. (2) and the simulated and measured object-image relation of the two metalenses. It is obvious that the wide-angle metalens has a nearly ideal object-image relation, and the narrow-angle metalens shows a large deviation. When the object distance y_1 is larger than 55 mm, the measured y_2 of the wide-angle metalens exactly follows Eq. (2). This is because the incident angle does not exceed 25° when $y_1 > 55$ mm, which is within the optimization range. In fact, the object-image relation conforms to the Gaussian formula to a good extent when y_1 is further reduced to 40 mm for the wide-angle design. In contrast, the deviation of the narrow-angle design from the ideal curve is increasingly severe with the decrease of the object distance.

Figure 5 further analyzes the off-axis object-image relation by shifting the relative position of the point source and the metalens along the x direction, as shown in Fig. 5(a). Here the object height is x_1, and the object distance is still y_1. By combining Eqs. (2) and (3), one can find the theoretical image height x_2 and image distance y_2 for any pair of (x_1, y_1),

$$x_2 = \frac{y_2}{y_1} x_1. \tag{3}$$

Here the point source is placed at the object distances of $2.5f$, $3f$, and $4f$, respectively. Figures 5(b) and 5(c) show the variation of x_2 and y_2 with x_1. The simulation agrees well with the theoretical result. In Fig. 5(b), the slope of the curve is defined as the magnification, which is larger for shorter object distance y_1. The

image distance does not change with x_1 in Fig. 5(c), meaning that the image is located in the same plane. In addition, the narrow-angle metalens cannot effectively focus the point source in the off-axis condition, so Fig. 5 only shows the results of the wide-angle metalens.

Finally, we insert a practical object in the collimated THz beam before it is launched to the metalens. The object is a metal concentric ring, as shown in Fig. 6(a). The diameters of the inner and outer rings are 19 and 33 mm, respectively, and the width of the ring is 2 mm, slightly less than the wavelength 2.14 mm. The object distance is $4f$. The simulated and tested images of the narrow-angle and wide-angle metalenses are summarized in Figs. 6(b)–6(e). The narrow-angle lens images the inner ring well. But the outer ring is very weak, and some light converges to the center, leading to the fake image. In contrast, the wide-angle metalens reconstructs the concentric rings well at the desired imaging distance. The image size and contrast match expectations. The tested image in Fig. 6(e) shows nonuniform intensity along the ring, which is attributed to the nonideal Gaussian beam radiation in the system. Despite the nonuniformity, this result still verifies the effectiveness of the wide-angle metalens in practical applications.

5. Conclusion

In this study, the metalens as a whole is optimized to enable the wide-angle focusing within ±25° at 0.14 THz. It shows stable focusing efficiency, constant FWHM, and diffraction-limited MTF with the increase of the incident angle. By tuning the relative distance of a point source and the metalens, the object-image relation is systematically tested, which follows the ideal Gaussian formula rule. This makes the thin flat metalens truly comparable to the traditional convex thin lenses in terms of imaging, and at the same time eliminates the off-axis aberration. The imaging result of the real object further proves its wide field of view and good imaging contrast for practical applications. One can further increase the field of view by taking more incident angles into the optimization. But the focusing efficiency may be sacrificed to some extent, which can be solved by increasing the number of layers and the number of ridges in the metalens design.

Fig. 6. (a) Experimental setup for practical object imaging with a close look at the object; image of the object by the narrow-angle metalens in (b) simulation and (c) experiment; image of the object by the wide-angle metalens in (d) simulation and (e) experiment.

References

1. N. Yu, P. Genevet, M. A. Kats, *et al.*, "Light propagation with phase discontinuities: generalized laws of reflection and refraction," Science **334**, 333 (2011).
2. Q. Song, S. Khadir, S. Vezian, *et al.*, "Bandwidth-unlimited polarization-maintaining metasurfaces," Sci. Adv. **7**, eabe1112 (2021).
3. F. Ding, Y. T. Chen, and S. I. Bozhevolnyi, "Metasurface-based polarimeters," Appl. Sci. **8**, 594 (2018).
4. M. R. M. Hashemi, S.-H. Yang, T. Wang, *et al.*, "Electronically-controlled beam-steering through vanadium dioxide metasurfaces," Sci. Rep. **6**, 35439 (2016).
5. P. Genevet and F. Capasso, "Holographic optical metasurfaces: a review of current progress," Rep. Prog. Phys. **78**, 024401 (2015).
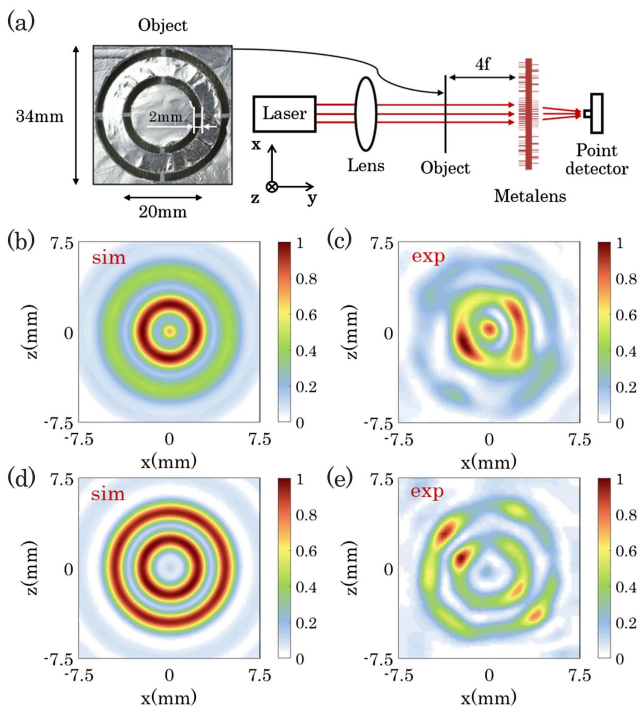
6. H.-H. Lv, Q.-L. Huang, X.-J. Yi, *et al.*, "Low-profile transmitting metasurface using single dielectric substrate for OAM generation," IEEE Antennas Wirel. Propag. Lett. **19**, 881 (2020).

7. X. Liu, S. Li, C. He, *et al.*, "Multiple orbital angular momentum beams with high-purity of transmission-coding metasurface," Adv. Theor. Simul. **6**, 2370010 (2023).

8. W. W. Liu, H. Cheng, J. G. Tian, *et al.*, "Diffractive metalens: from fundamentals, practical applications to current trends," Adv. Phys. X **5**, 1742584 (2020).

9. M. L. Tseng, H. H. Hsiao, C. H. Chu, *et al.*, "Metalenses: advances and applications," Adv. Opt. Mater. **6**, 1800554 (2018).

10. D. Hu, X. Wang, S. Feng, *et al.*, "Ultrathin terahertz planar elements," Adv. Opt. Mater. **1**, 186 (2013).

11. X. Jiang, H. Chen, Z. Y. Li, *et al.*, "All-dielectric metalens for terahertz wave imaging," Opt. Express **26**, 14132 (2018).

12. F. Zhao, Z. Li, X. Dai, *et al.*, "Broadband achromatic sub-diffraction focusing by an amplitude-modulated terahertz metalens," Adv. Opt. Mater. **8**, 2000842 (2020).

13. T. Suzuki, K. Endo, J. Kim, *et al.*, "Metalens mounted on a resonant tunneling diode for collimated and directed terahertz waves," Opt. Express **29**, 18988 (2021).

14. J. He, T. Dong, B. Chi, *et al.*, "Metasurfaces for terahertz wavefront modulation: a review," J. Infrared Millim. Terahertz Waves. **41**, 607 (2020).

15. X. Dong, J. Cheng, Y. Yuan, *et al.*, "Arbitrary large-gradient wavefront shaping: from local phase modulation to nonlocal diffraction engineering," Photonics Res. **10**, 896 (2022).

16. Z. Wang, Q. Li, and F. Yan, "A high numerical aperture terahertz all-silicon metalens with sub-diffraction focus and long depth of focus," J. Phys. D Appl. Phys. **54**, 085103 (2020).

17. H. Chen, Z. Wu, Z. Li, *et al.*, "Sub-wavelength tight-focusing of terahertz waves by polarization-independent high-numerical-aperture dielectric metalens," Opt. Express **26**, 29817 (2018).

18. Z. Wu, J. Zhu, Y. Zou, *et al.*, "Superoscillatory metalens for polarization conversion and broadband tight focusing of terahertz waves," Opt. Mater. **123**, 111924 (2022).

19. C. Qin, W. Fan, Q. Wu, *et al.*, "Polarization insensitive achromatic terahertz metalens based on all-dielectric metasurfaces," Opt. Commun. **512**, 128061 (2022).

20. Q. Cheng, M. Ma, D. Yu, *et al.*, "Broadband achromatic metalens in terahertz regime," Sci. Bull. **64**, 1525 (2019).

21. Y. Xu, J. Gu, Y. Gao, *et al.*, "Broadband achromatic terahertz metalens constituted by Si–SiO$_2$–Si hybrid meta-atoms," Adv. Funct. Mater. **33**, 2302821 (2023).

22. J. Cheng, Y. Yang, F. Fan, *et al.*, "Terahertz tight-focused Bessel beam generation and point-to-point focusing based on nonlocal diffraction engineering," Opt. Lett. **47**, 2879 (2022).

23. X.-Q. Jiang, W.-H. Fan, L.-R. Zhao, *et al.*, "Continuously varifocal metalens for broadband achromatic focusing of terahertz waves," J. Sci. Adv. Mater. Devices **8**, 100560 (2023).

24. A. Arbabi, E. Arbabi, S. M. Kamali, *et al.*, "Miniature optical planar camera based on a wide-angle metasurface doublet corrected for monochromatic aberrations," Nat. Commun. **7**, 13682 (2016).

25. X. Dong, J. Cheng, F. Fan, *et al.*, "Efficient wide-band large-angle refraction and splitting of a terahertz beam by low-index 3D-printed bilayer metagratings," Phys. Rev. Appl. **14**, 014064 (2020).

26. Y. Yang, J. R. Cheng, X. P. Dong, *et al.*, "3D high-NA metalenses enabled by efficient 2D optimization," Opt. Commun. **520**, 128448 (2022).